Journal of Materials Chemistry A

Metastable oxysulfide surface formation on LiNi$_{0.5}$Mn$_{1.5}$O$_4$ single crystal particles by using carbothermal reaction with Sulfur-doped hetercarbon nanoparticles: New insight for their structural and electrochemical characteristics, and their potential applications

Journal:	*Journal of Materials Chemistry A*
Manuscript ID	TA-ART-08-2020-007622.R1
Article Type:	Paper
Date Submitted by the Author:	25-Sep-2020
Complete List of Authors:	Kim, Dae-wook; Shinshu University, Department of Materials Chemistry Zettsu, Nobuyuki; Shinshu University, Center for Energy & Environmental Science Shiiba, Hiromasa; Shinshu University, Department of Materials Chemistry Sánchez-Santolino, Gabriel; The University of Tokyo, Institute of Engineering Innovation Ishikawa, Ryo; The University of Tokyo, Institute of Engineering Innovation Ikuhara, Yuichi; The University of Tokyo, Institute of Engineering Innovation, School of Engineering; Japan Fine Ceramics Center, Nanostructures Research Laboratory Teshima, Katsuya; Shinshu University, Department of Materials Chemistry; Shinshu University, Center for Energy and Environmental Science

SCHOLARONE™
Manuscripts

ARTICLE

Metastable oxysulfide surface formation on LiNi$_{0.5}$Mn$_{1.5}$O$_4$ single crystal particles by using carbothermal reaction with Sulfur-doped hetercarbon nanoparticles: New insight for their structural and electrochemical characteristics, and their potential applications

Dae-wook Kim,[a] Nobuyuki Zettsu,[a,b,]* Hiromasa Shiiba,[b] Gabriel Sánchez-Santolino,[c] Ryo Ishikawa,[c,d] Yuichi Ikuhara,[c] and Katsuya Teshima [a,b,]*

Spinel LiNi$_{0.5}$Mn$_{1.5}$O$_4$ (LNMO) and related compounds have been attractive much attention as a high voltage cathode material for lithium ion batteries, however, their strong Lewis basic characteristics shown at the surface promotes various side reactions in associating with the oxidative decomposition of the electrolyte, leading to significant capacity degradation as increase of cycle numbers. We have proposed multi-anion surfaces (such as oxyfluoride) for direct tuning of the electronic properties for cathode surface. In this study, we report the synthesis of LNMO single crystals with oxysulfide surface and characterization of their electrochemical properties. Carbothermal reaction at around 450°C with sulfur-doped hydrocarbons (S-HC) nanoparticles as a solid-phase precursor made it possible to prepare metastable oxysulfide surface without excess-reduction of transition metals in the spinel frame. This systematic study, using experimental and theoretical approaches, revealed many new findings for understanding the oxysulfide surface effects. The incorporated S^{2-} were preferentially occupied at O^{24e}-sites ($P4_332$), which are bonded with three transition metals containing single Ni^{2+} and double Mn^{4+}, leading to mitigating cation mixing of Li$^+$/Ni^{2+} formed at the surface and reducing surface energy of {100} faces, resulted in significant changes in the corresponding electric structures, large morphological changes and an increase of specific capacity, as well as significant cyclability enhancement. Furthermore, it was found that the S-2p orbital was newly appeared at a higher level than the Ni-3d orbital, resulting in the dramatic changes of their electrical properties, including narrowed their band gap and lowered overpotential for the redox reaction of Ni^{2+}/Ni^{3+}.

Introduction

Rechargeable batteries are crucial devices that support our current daily life through energizing smartphones, tablets, laptops, wearable appliances, power tools, and many other applications. They are becoming increasingly important as energy storage devices for electric and hybrid vehicles, as well as energy storage devices for energy management systems combined with renewable energy generators. Furthermore, these battery systems are a key technology for limiting carbon dioxide emissions and addressing climate change. Research on LIBs has been attracting worldwide attention, despite there being many candidates for electrical conversion systems including fuel cell and Li-ion, Ni metal hydride, and lead-acid batteries. For

mounting on electric vehicles, however, there are many technical limitations such as higher energy density of ca. 700 Wh/L with pouch cell (corresponding gravimetric energy density is ca. 300 Wh/kg) while maintaining long-term stability (100,000 miles for 8 years), safety, and cost of <$100/Wh[1–4].

The energy density of a given battery is determined by its working voltage, specific capacity, and electrode density. In particular, the increase of the operational voltage corresponding to the redox potential for the intercalation reaction of Li$^+$ at the cathode above 4.45 V (vs Li$^+$/Li) represents one of the most serious issues for high-energy-density LIBs. Because lowering the level of the *d* band occupied by the electrons of the transition metal component of the cathode noticeably increases its redox potential, layered materials with high Ni contents (such as NCM811 and NCA) have attracted significant attention.

Among these cathode materials, high-voltage spinels, LiNi$_{0.5}$Mn$_{1.5}$O$_4$ (LNMO) and related compounds, have also been considered for this purpose due to the absence of Co element, ability to be easily handled in air, thermal stability, and existence of a robust spinel framework after full delithiation[5-7]. Recently, Manthiram et al. reported an overview of the recent developments on understanding various factors that influence the electrochemical performance of high-voltage spinel cathodes[8]. The authors clarified that factors such as the degree

a. *Department of Materials Chemistry, Shinshu University, 4-17-1 Wakasato, Nagano, 380-8553, Japan*
b. *Research Initiative for Supra-Materials, Shinshu University, 4-17-1 Wakasato, Nagano, 380-8553, Japan*
c. *Institute of Engineering Innovation, The University of Tokyo, Tokyo, 113-8656, Japan*
d. *Japan Science and Technology Agency, PRESTO, Kawaguchi, Saitama 332-0012, Japan*
† Footnotes relating to the title and/or authors should appear here.
Electronic Supplementary Information (ESI) available: [details of any supplementary information available should be included here]. See DOI: 10.1039/x0xx00000x

of cation ordering, Mn^{3+} content, morphology, and surface planes/compositions are influenced by synthesis and annealing conditions. For example, samples with a {111} family of surface planes show superior performance compared to that with other planes[9,10]. However, their high operating voltages (>4.4 V vs. Li^+/Li) commonly result in the oxidative decomposition of the electrolyte at highly delithiated LNMO electrode surface bearing strong Lewis basic characteristics, which subsequently promotes various side reactions, including Mn^{2+} elution, the formation of metal fluorides, and excessive growth of solid–electrolyte interface (SEI) deposition[11–13]. There have been many approaches that have attempted to mitigate the observed capacity fading of LNMO/graphite full cells, such as reduction of the direct contact area of the cathode with the electrolyte through coating with inorganic particles and molecules as well as by adding organic modifiers to the electrolyte[14–22]. More generally, organic coating strategies based on the introduction of small molecule additives into the electrolyte have been widely used to protect the electrode surface of conventional LIB cells with an operating voltage of less than 4.45 V (vs Li^+/ Li). However, these approaches provide only limited performance enhancements in LNMO/graphite full cells, considering the electrochemical dilemma exhibited by the oxidative and reductive degradation of the electrolyte governed by the HOMO-LUMO analogy[23-26]. For example, it is known that vinylene carbonate (VC) molecules as a typical additive provide stable SEI layer formation on the graphite anode surface via a decomposition reaction and lead to good cycling performance. However, it cannot effectively protect the capacity fading of graphite anode coupled with LNMO cathodes as the cycle number increases because VC molecules do not show enough durability to oxidation at 4.7 V (vs Li^+/Li). Excess SEI layer formation occludes active sites by the oxidative decomposed products generated at the LNMO cathode surface.

Recently, we have demonstrated the stabilization of LNMO electrode surface via the direct ionic potential tuning (HOMO level engineering). Surface modification of the LNMO electrode with a self-assembled monolayer of fluoroalkylsilane molecules or fluoride anion (F^-) incorporation into the oxygen deficient formed on the surface (F_{Vo}) have been proposed as strategic approaches for overcoming the above limitations[27-29]. For example, the oxyfluoride surface significantly improved both C rate capability and cyclabilities, however, the coordination bond formation of F-Mn^{3+}-F in the oxyfluoride surface layer provided specific capacity degradation compared to the theoretical capacity. Our DFT calculation and XAFS measurements strongly suggested that the incorporated two F^- ions preferentially coordinate to single Mn^{3+} ions (MnO_4F_2 octahedral) promoted the electrochemical inactivation of Mn^{3+} via the stabilization of their Jahn-Teller distortion along the b-axis orientation. As their oxidation potential increased up to 5.2 V (vs Li^+/Li), it was found that some lithium ions in the fluorinated LNMO lattice could not be completely delithiated during charging, which caused a decrease in capacity[29].

Many fundamental studies have been conducted on cation substitution effects in oxide-based functional materials sciences, another approach for stabilizing the electrochemical performance of cathode materials that has recently been gaining more attention is anion doping[30,31,32]. This is likely to be limited by the temperature required for introducing the anionic species into the oxide framework (not physisorption). Halide ions (F^-, Cl^-) can be incorporated into target crystal lattices at a relatively lower temperature by a solid-state reaction[33], reaction with XeF_2 gas phase[34], or reaction in molten salts[29]. Conversely, the synthesis of oxysulfides, oxynitrides, and other many possible multi-anion systems generally requires high temperature (>800 °C) under an oxygen-deficient atmosphere for the synthesis due to use of gas phase anion sources. However, it leads to a difficulty in suppressing the reduction reaction of transition metals ions contained in active materials to their metallic form, i.e., state with zero oxidation number. In order to understand the full aspects of the multi-anion surface effects on the side reaction that appeared at the electrolyte interface as well as the diffusion behavior of Li^+ inside the electrodes, finding a new synthesis route with a lower temperature of at least below 600 °C is necessary.

In this literature, as one of the multi-anion surface engineering approaches, we are studying the effects of the incorporation of S^{2-} on the structure and electrochemical properties of high voltage LNMO spinel for the first time in the world. We aimed to reveal the impact of the physical properties, delivered by incorporating S^{2-} which has different ionic radius, electronegativity, and charges, as comparing to those of O^{2-}. Our newly developed carbothermal reaction, using sulfur-doped amorphous hydrocarbon powders as a solid sulfur source, made it possible to prepare an oxysulfide surface, and both experimental and theoretical results provided many new findings of the oxysulfide surface effects on both structural and electrochemical characteristics in high-voltage spinel LNMO electrodes.

Experimental Section

Preparation of the LNMOS$_x$ electrode. Sulfur-doped amorphous hydrocarbon (S-HC) powders were synthesized by a solution plasma process (SPP). Nonequilibrium cold plasma in an aromatic solvent resulted in the formation of amorphous nanocarbon powder having a disordered phase[35]. The schematic illustration of the SPP setup is presented in the Fig. S1. In this study, a thiophene (C_4H_4S) was used as a precursor. A bipolar pulsed generator (Kurita Manufacturing Co., Ltd., MPP04-A4-30) was used as a power supply for making glow discharge in thiophen. The applied voltage and pulse width were 1.6 kV and 2 μs, respectively. The obtained suspension was filtrated and dried in a vacuum oven at 100 °C. Eventually, 1 g of black powder was obtained after discharge for 1 h. $LiNi_{0.5}Mn_{1.5}O_4$ (LNMO) crystals were prepared by flux growth using LiCl–KCl mixed molten salt[28.] The obtained S-HC powders were grinded with LNMO crystals in a mortar by hand milling for 20 min. Then, the mixture was placed in an alumina crucible with 30 mL volume. The S-HC concentration was adjusted to 10 and 15 mol% for S^{2-} incorporation. The mixture was heated in an electric furnace at 600 °C under static air atmosphere. After maintaining temperature for 3h, the mixture was cooled to 500 °C. Then it was cooled to room temperature naturally in the furnace.

Characterization Morphological characteristics were evaluated by using field emission scanning electron microscopy (FE-SEM,

JSM-7600F at 10 kV; JEOL, Japan). The crystal phases were examined by X-ray diffractometer (XRD) with a Cu-Kα source. X-ray diffraction (Miniflex II, Rigaku, Japan) measurements were conducted at 30 kV and 20 mA with a scan range of $2\vartheta = 10$–$80°$. The chemical compositions and chemical states were characterized using inductively coupled plasma optical emission spectroscopy (ICP-OES, Hitachi High-Tech Science Corp., Japan, SPS5510), X-ray photoelectron spectroscopy (XPS, JEOL Ltd., Japan, JPS-9010MX; 15 kV, 15 mA, monochromic Al K_α source), and ultraviolet photoelectron spectroscopy in atmospheric pressure (UPS, RIKEN KEIKI CO. Ltd., Japan, AC-3; 10 nW, Deuterium lamp, N_2 substitution type grating monochromator). The cation (Ni, Mn) arrangements were evaluated by Raman spectroscopy (LabRAM, Horiba Ltd., Japan, 532 nm excitation). An original atomic surface structure was characterized by atomic-resolution scanning transmittance electron microscopy (STEM). The LNMOSx powders in ethanol were dispersed on a perforated amorphous carbon grid supported by Cu mesh. The atomic-resolution annular dark-field (ADF) STEM images were acquired by an aberration-corrected JEM ARM300CF instrument (JEOL, Ltd.) installed at the University of Tokyo, equipped with a cold-field emission gun and electron energy-loss spectroscopy (EELS, Quantum, Gatan Inc.). To suppress the beam damage to Li-containing materials, we operated the microscope at 80 kV with a relatively low beam current of ~10 pA, where no significant structure changes were observed during image acquisition. The convergence semi-angle was 30 mrad, and the collection semi-angle for ADF-STEM is 72-200 mrad. The electrochemical properties were evaluated using a R2032-type coin cell. The cathode was composed of active materials, acetylene black, and polyvinylidene fluoride (PVDF) in the weight ratio of 90:5:5. The mixture was mixed with N-methyl-2-pyrrolidone (NMP) to give a viscosity of ~5.1 Pa·s. The prepared paste was coated onto an Al foil (Al foil thickness is ca. 20 μm) using a baker type applicator. The mass of cathode materials was controlled to be ca. 10 mg/cm². All electrodes were dried at 120 °C in vacuum for 24 h prior to use. A porous polypropylene film (#2500, Celgard) was used as a separator. Next, 1 M $LiPF_6$ mixed with ethylene carbonate and dimethyl carbonate (EC-DMC, 3:7 vol.%) was used as an electrolyte and 2030 type coin cells were assembled in an Ar-filled glovebox (MDB-2BL, Miwa Mfg Co., Ltd., Japan) with a controlled atmosphere ($\leq$ 1 ppm of H_2O and O_2). The galvanostatic charge–discharge test was conducted using a galvanostat (HJ1020Msd8, Hokuto Denko, Japan) in a voltage range of 3.5–4.8 V (vs Li⁺/Li). The electrochemical impedance spectroscopy (EIS) and cyclic voltammetry (CV) measurements were performed using an electrochemical workstation (VSP-300, Bio-logic, France) in a frequency range of 2 MHz–1 mHz for EIS and voltage range of 3.5–5.0 V at a scan rate of 0.15 mV/s for CV, respectively. All electrochemical measurements were performed in a chamber with a controllable constant temperature (SU-221, Espec, USA) of 25 °C. Equivalent circuit model was used for the evaluation of impedance parameters:
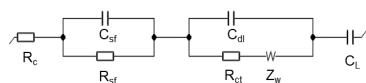
Galvanostatic intermittent titration technique (GITT) was performed at 0.2C using an electrochemical workstation (VSP-

300, Bio-logic, France). The both LNMO /Li and LNMOS$_{0.15}$/Li cells were charged for 10 min and then followed by a relaxation time of 60 min between 3.5 and 4.8 V. The Li+ diffusion coefficient (D$_{Li}$) was calculated by using a following equation:

$$D_{Li} = \frac{4}{\pi\tau}\left(\frac{mV_m}{MA}\right)^2\left(\frac{\Delta E_s}{\Delta E_\tau}\right)^2$$

τ is the constant current flux time. V_m (cm³ mol⁻¹) is the molar volume of the LNMO crystals, M (g mol⁻¹) and m (g) are the molecular weight and mass of the cathode material, respectively. A (cm²) is the area of the electrode, ΔE_τ and ΔE_S is the steady voltage-change after the relaxation period and the total voltage-change during the single titration current flux, respectively.

DFT calculation The DFT calculations were performed using the generalized gradient approximation (GGA-PBEsol) + U and projector-augmented wave methods as implemented in the Vienna ab initio simulation package (VASP).[36–38] The U values for the d-orbitals of Ni and Mn were set to 6.0 and 3.9 eV, respectively.[39–41] The magnetic ground state of LNMO exhibits ferrimagnetic ordering (Ni↓Mn↑), as reported in previous experimental and computational studies[30,42–44]. Thus, the ferrimagnetic spin configurations were used for all the calculations in this study. An energy cut-off of 500 eV and a 3 × 3 × 3 k-point mesh was used for the superstructure of 56 atoms in a cubic spinel lattice of 8($LiNi_{0.5}Mn_{1.5}O_4$) with $P4_332$ symmetry as a starting structure. To realize the atomic arrangement of 8($LiNi_{0.5}Mn_{1.5}O_{4-x}S_x$) (x =0.125, 0.25), we added one or two sulfide anions into the possible 24e and 8c O oxygen sites in the unit cell. The nudged elastic band method was used to investigate the minimum energy pathways of lithium hopping from one lattice position to adjacent sites[45]. Relaxation of the crystal structure was allowed for all calculations, and the final energies of the optimized geometries were recalculated to correct for changes of the plane-wave basis during relaxation. We manually arranged the atoms on the LNMO surface while retaining their crystallographic symmetry and chemical stoichiometry for calculating the energy of a slab with a surface facet. The crystallographic symmetry of the top and bottom slab surfaces is essential for achieving a rational computational prediction. The slab cells were constructed from the relaxed bulk structure, and the lattice parameters were fixed for the slab cells. For the calculations of the surface facets, slab thicknesses greater than 20 Å were chosen for all facets with vacuum thicknesses of 20 Å. For the calculation of sulfur defect on the surfaces, single S^{2-} ion was substituted on the terminated O^{2-} ion at (100) and (100) faces in stoichiometric LNMO.

Results and discussion

The S^{2-} defect formation energy in $LiNi_{0.5}Mn_{1.5}O_{4-x}S_x$ for x = 0.125 ($Li_8Ni_4Mn_{12}O_{31}S_1$) and x = 0.25 ($Li_8Ni_4Mn_{12}O_{30}S_2$) were analyzed by DFT calculation. Each atom in $P4_332$ LNMO occupies $\{(Li)^{8c}\}_{tet}\{(Ni_{0.5})^{4b}(Mn_{1.5})^{12d}\}_{oct}(O)^{8c}(O_{3-x})^{24e}(S_x)^{24e}$, where superscripts indicate Wyckoff notation and subscripts tet and oct indicate tetrahedral and octahedral sites, respectively (Fig. S2). The LNMOS with an S^{2-} composition of 0.25 contains two S^{2-} in the superlattice consisting of 56 atoms. Therefore, the model of the first-principles calculation is well covered to the local structure of

the experimentally obtained oxysulfide composition. However, we have not considered relaxation process sometimes happening at surface. We performed the formation energy calculation of which single and/or double S^{2-} defects were formed in the superlattice. As shown in Table S1, the all defect formation energies are negative, implying that the incorporated S^{-2} are thermodynamically unstable in the LNMO lattice. This computational finding highlights that the synthesis of an oxysulfide LNMO is highly difficult using thermodynamically controlled reactions.

Nonequilibrium cold plasma discharged in thiophene resulted in the formation of black powders. FE-SEM observation revealed that the black particles formed spherical shapes with 20-30 nm diameter (Fig. S3a). Their powder XRD profile suggested that the particles formed an amorphous phase (Fig. S3b). We quantified the oxygen and sulfur contents in atomic % by using XPS measurement for conducting chemical composition. The measured contents in at% was converted to mol% and chemical composition. Corresponding XPS quantification table were shown in Table S2. It clearly revealed that the sulfide anion was atomically incorporated in the amorphous carbon matrix. According to previous reports, high amounts of oxygen and hydrogen were also included in the matrix, implying that the S-HC particles will support combustion in the following reaction under air at a high temperature[35].

The incorporation of S^{2-} into LNMO lattice was performed through the carbothermal combustion reaction, initialed with the S-HC particles. A typical TG-DTA profile of the mixture was composed of LNMO crystal and S-HC particles (Fig. 1a). Exothermic peak was detected at approximately 450 °C. When only the particles were heated alone, a sharp exothermic peak was not clearly observed. It may have caused a combustion reaction of the S-HC particles, catalyzed by the LNMO crystal surface. The powder XRD profiles for LNMO and LNMOS$_x$ crystals are displayed in Fig. 1(b). As all diffraction lines can be assigned to reference data (ICDD PDF 70-8650) with small shifting, LNMOS$_x$ crystals presented single phase without significant subphase formation by a combustion reaction. The lattice parameter was increased as the S^{2-} substitution due to different ionic radius between O^{2-} (1.26 Å) and S^{2-} (1.70 Å) anions. The chemical compositions were evaluated by ICP-OES and XPS for cations and anions, respectively (Table S2). For convenience, the obtained crystals were denoted as LNMOS$_{0.1}$ and LNMOS$_{0.15}$. We further examined the depth profiles of XPS-S3p core-level spectral as a function of Ar sputtering times (Fig. 1c). The XPS signal assigned to oxysulfide detected from the LNMOS$_{0.1}$ crystal surface became extremely weak to the lower detection limit level taken from the 20 nm etched surface. The remarkable changes in the depth profile indicated that S^{2-} were locally incorporated at the crystal surface. Furthermore, because the reaction did not proceed to the inside of the crystal, this finding strongly supports that the S^{2-} incorporating reaction was instantaneously progressed under combustion reaction.

The impact of surface oxysulfidation on $Li^+/Ni^{2+}/Mn^{4+}$ cations arrangement in LNMO lattice was studied using Raman spectroscopy (Fig. 1d). LNMOS$_x$ crystals presented no significant changes in spectral features with LNMO crystals in contrast to that of F^- substitution. Intense Raman signals at 402, 495, and 642

cm^{-1} can be assigned to Ni–O stretching bond for 402 and 495 cm^{-1}, and Mn–O stretching bond for 642 cm^{-1}. Moreover, peak splitting observed at 507–606 cm^{-1} and 220–240 cm^{-1} were evidentiary characteristic peaks which implies that the spatially $P4_332$-type cation arrangement was formed inside the LNMOS$_x$ crystal.

Supplementary Fig. S2a, b shows the most stable atomic arrangements in LiNi$_{0.5}$Mn$_{1.5}$O$_{4-x}$S$_x$ analyzed by DFT calculation for (a) x = 0.125 (Li$_8$Ni$_4$Mn$_{12}$O$_{31}$S$_1$), and (b) x = 0.25 (Li$_8$Ni$_4$Mn$_{12}$O$_{30}$S$_2$), respectively. The S^{2-} was preferentially occupying O-sites (24e sites instead of the 8c sites) which are bonded with three transition metals containing single Ni^{2+} and double Mn^{4+}, irrespective of the number of incorporations. Lattice constant and corresponding lattice volume was increased as the incorporation of S^{2-} which was accorded with XRD data (Fig. 1b). No calculational evidences on O^{2-}/S^{2-} anion ordering arrangements in LiNi$_{0.5}$Mn$_{1.5}$O$_{3.75}$S$_{0.25}$ lattice were obtained, it implies that S^{2-} ions occupy randomly in the anion sublattice. Their formation energy in most stable atomic arrangements and 10th stable arrangement has little energy difference of 25 meV f.u^{-1}. Furthermore, DFT calculation suggests that any -S^{2-}-S^{2-}-clusters were impossibly formed in the cubic LNMO systems due to its large ionic radius. MO6 (M=Ni, Mn) octahedron accept only a single S^{2-}. These results on local transition metal arrangement (Fig. 1d) and anion ordering characteristics (Fig. S2) are distinctly different from the previously reported oxyfluorinated spinel LNMOF$_x$.[30] It is related to the fact that the S^{2-} has the same divalent anion as the O^{2-} and may not have required a charge-neutralization response for Mn^{4+} to Mn^{3+} via oxysulfide surface formation.

In contrast, surface oxysulfidation resulted in the drastic morphological changes. FE-SEM observation clearly visualized the truncation at the corners and edges of the parental octahedral structure of LNMO crystals (Fig. 1e). The truncated faces were assigned to the {100} faces, bearing a higher surface energy than the {111} face. Thus, the incorporated S^{2-} potentially made the surface energy of the {100} faces lower, compared to the standard LNMO crystal surface. The truncation was enhanced by the amount of incorporated S^{2-}. Fig. 2a-c show ADF-STEM images of the LNMOS$_x$ surface viewed along the [110] direction. There are two-types of surfaces as {100} and {111}, which is consistent with FE-SEM observations. Owing to Z-contrast nature (Z is atomic number), the heavy atom-containing column becomes brighter. At the {111} facet plane, the brighter contrast appears in the Li sites. It suggests that the transition metals of Mn and / or Ni at the octahedral 12d or 4b site migrate to tetragonal Li 8c site as antisite defects formation, although the thickness is very thin as one-unit cell. A similar result was observed at the {100} surface. The transition metals were transferring to the Li site from the original site. The reconstructed surface thickness composed of different atomic arrangements became slightly thicker as three or four unit-cells. DFT calculation on the formation energy of anti-site spinel structures at both facet surfaces of {111} and {100} also supports the movable Li ions is lacking within a few unit-cells from the surface via anti-site defect formation.

Fig 2d, e shows the Mn oxidation state as a function of distance from the surface to the bulk, where we quantified the Mn-L2,3

edge. The Mn oxidation state is substantially reduced at the reconstructed surface down to less than Mn^{3+}. Unfortunately, we did not directly figure out the atomic arrangement of incorporated S^{2-} inside the crystal by STEM observation. The mechanism for the change in the valence state of Mn in association with O^{2-} and S^{2-} vacancies formation in the reconstructed surface has been not cleared at this state. It cannot be denied that oxygen and sulfur may have desorbed from the crystal surface due to electron beam excitation during microscopic observation. Another possibility is that the reconstructed structures in the surface region is considered to have been formed by removing half of the atoms to mitigate the dipole moment formed on polar {100} and non-polar {111} planes of $LNMOS_x$ crystals during the oxysulfide surface formation.[46] This theory can explain the difference in reconstructed surface thickness between the {100} and {111} planes. Furthermore, our DFT calculation suggests that the S^{2-} defect formation energy for stoichiometric {100} faces (-0.28 eV) shows significantly smaller than that of {111} faces (0.07 eV) in $LiNi_{0.5}Mn_{1.5}O_4$.

Galvanostatic charge-discharge tests at various C rates were systematically performed to examine the effect of the S^{2-} substitution on the kinetical parameters in association with Li^+ diffusion behaviors. Fig. 3a shows the third charge-discharge cycle profiles at 30 $mA·g^{-1}$, corresponding to a 0.2 C rate. The S^{2-} substitution slightly affected the voltage slope characteristics. The continuous gentle changes in the flat voltage starting from 4.6–4.8 V (vs. Li^+/Li) were observed for all half-cells. These slops were assigned to the intercalation reaction based on a two-phase reaction mechanism in association with the redox couples of Ni^{2+}/Ni^{3+} and Ni^{3+}/Ni^{4+}. Moreover, it was indicative of spatial $Li^+/Ni^{2+}/Mn^{4+}$ ordering in spinel frameworks, which led to $P4_332$ symmetry formation, which agrees with the results of Raman spectroscopy. A distinct inflexion point in the voltage slope at around 3.8 V was detected for the $LNMOS_x/Li$ half-cells. Since the increased capacity based on the S^{2-} incorporation contributed to less than 10% of total capacity, it might be reflected by the atomic rearrangement formed inside the top 10 nm-thick crystal surfaces, as shown by XPS and EELS measurement coupled with STEM observation. Notably, our DFT calculation suggests a plausible mechanism for explaining the origin of the distinct inflexion point. The changes in the most stable atomic structure of $LNMOS_x$ as a function of their lithium composition were computed using the formation energies of $P4_332$-type $LNMOS_x$ with different atomic arrangements (Fig. S4). In Figure S4 and Fig. 3b, we have showed the changes in atomic arrangements in delithiation reaction, yielded corresponding voltage slopes computationally. We evaluated formation energies of the all possible atomic arrangements for each $LNMOS_x$ with different Li compositions. These figures plotted vertically the formation energies of the all possible atomic arrangements. Thus, the bottom one aligned on the y axis means the minimum formation energy of the most candidate thermodynamically stable atomic arrangement. Furthermore, the changes in atomic arrangements, in association with delithiation reaction, yielded corresponding voltage slopes and corresponding reaction mechanism as well as the structural transitions, computationally. As shown in Fig. 3b, the above DFT calculation provided computationally-duplicated voltage profile of the charging process from 3.5–5.0 V. The LNMO electrode showed a flat voltage at delithiation at ~4.7 V, assigned

to the oxidation of Ni^{2+} to Ni^{4+}, whereas the $LNMOS_x$ electrodes displayed distinct plateaus at ~4.7 V and an additional small plateau at around 3.8 V. $LNMOS_{0.125}$ showed that there was no intermediate phase in delithiation process from $L_{1.0}NMOS_{0.125}$ to $L_{0.875}NMOS_{0.125}$ and from $L_{0.875}NMOS_{0.125}$ to $L_0NMOS_{0.125}$. Furthermore increase of the S^{-2} incorporation extended to the first two-phase model regions up to $L_{0.75}NMOS_{0.250}$, indicating that the two kinds of two-phase regions coexist during the delithiation process, which correspond to the oxidation of Ni^{2+} to Ni^{4+} in the charge process. Fig. 3c and d indicates the calculated partial densities of state diagrams (PDOSs) for Mn 3d, Ni 3d, and S 3p bands in $P4_332$-type $LNMOS_{0.125}$ and $LNMOS_{0.25}$ with different lithium compositions, respectively. The Fermi level was set to be zero position in this these PDOSs. The changes in PDOSs, with respect to the change in lithium ion composition, provide insights regarding the oxidation reaction of transition metals that contribute to the electrochemical delithiation reaction. The PDOS profiles in the Mn 3d (Mn^{4+}) did not change during delithiation process. This indicates that their contribution to the oxidation reaction is significantly small. In contrast, the PDOS profiles of Ni^{2+} and S^{2-} simultaneously showed a drastic change when the lithium composition was reduced from $L_{1.0}NMOS_{0.125}$ to $L_{0.875}NMOS_{0.125}$. Hence, Ni^{2+} coordinated with S^{2-} were oxidized preferentially to Ni^{3+} during the early delithiation reaction step. In addition, it was found that Li^+ ions occupying the 4a site located closest to S^{2-} ions that occupy the 24e site preferentially deintercalated from the spinel lattice as the electrochemical oxidation of Ni^{2+} occurred at an applied voltage of 3.8 V. This oxidation potential is considerably lower than that at other sites of Ni^{2+} in the spinel lattice (ca. 4.7 V). Thus, Li^+ ions occupying the 4a site located closest to S^{2-} ions occupying the 24e site became unstable. Although not adequately clarified at this stage, we consider that the anti-site defects of Li^+/Ni^{2+} formed on the LNMO crystal surface was recovered by introducing S^{2-} on the surface. The lithium ions that reoccupied the original site are considered to become movable ions for electrochemical intercalation, and thus it contributes to the specific capacity improvement observed in LNMOS systems.

The effects of S^{2-} incorporation on reaction kinetics were further probed by subjecting half-cells to cyclic voltammetry (CV) measurements, C rate testing, and DFT calculation. As shown in Fig. S5, a broadened oxidative wave at 4.6–4.8 V associated with splitting peaks was observed for $LNMOS_x$ electrodes, and the polarization reduction were observed with an increasing amount of S^{2-} incorporation. The above behavior was ascribed to the presence of Ni^{2+}/Ni^{3+} and Ni^{3+}/Ni^{4+} redox pairs, which was also believed to account for the voltage step in the low-Li-content region of voltage profiles. These trends strongly imply that the S^{2-} incorporation potentially narrows the potential gap for step redox reactions of $Ni^{2+}/Ni^{3+}/Ni^{4+}$. The kinetics of Li^+ migration was examined by systematic galvanostatic charging-discharging tests at varying current densities (Fig. 4a). A small variation in discharge capacity presented within 10 mAh/g at a current density of 0.2 C was gradually increased as the current density rose. The $LNMOS_{0.15}$ electrode achieved the highest discharge capacity at a current density of 10 C. The specific capacities of $LNMOS_{0.1}$ and $LNMOS_{0.15}$ cathodes based half-cells at 10 C were determined as 30 and 40 $mAh·g^{-1}$, respectively. Even though both the loading amount (ca. 10 mg/cm^2) and tap density (ca. 3.0

g/cm³) were relatively high, these C rate characteristics do not provide sufficient evidence that LNMOS$_x$ crystals deliver superior C rate characteristics compared to other LNMO-related materials. For example, a fluorine-substituted oxyfluoride (LNMOF$_x$) electrodes showed much better rate capabilities which was attributed to both d-electron doping in Mn $3d$ band and the reduction of energy barrier for Li$^+$ hopping along energetically preferable 8a–16c–8a route inside of LNMO lattice with Fd-$3m$ symmetry. However, what is important in this paper is that the rate capabilities were improved by the S^{2-}substitution, as compared to that of pristine LNMO. The CV diagrams taken from the series of LNMOS$_x$ electrodes suggests that the current density, in association with kinetical parameters based electrochemical redox reaction of Ni^{2+}/Ni^{3+}/ Ni^{4+}, was highly enhanced. This is evidentially supporting the C rate capability enhancement trends.

The improved C rate capability observed in LNMOS$_x$ electrodes might be primarily attributed to thinner SEI layer formation on the electrode surface via the mitigation of side reaction happened at the electrolyte interface, driven by the oxysulfide surface (described details later). We further think that the enhancement in the electronic conductivity of LNMO crystals will deliver positive impacts on the C rate capability. Figure S6a shows orbital electronic structures of Mn-3d, Ni-3d, O-2p, and S-3p in some MO$_6$/ MO$_5$S octahedrons in LNMOS$_x$. These are almost same data of fully lithiated LNMOS$_x$ displayed in Fig.3 (c) and (d), except for their zero reference. To make it easier to intuitively understand the effect of S substitution on the changes in the bandgap of LNMOS$_x$, the value on the x-axis was re-edited based on the vacuum level. The S-3p orbital in the LNMOS$_x$ was appeared at higher energy level than the Ni-3d orbital of LNMO. It made the Fermi level higher, and smaller band gap of LNMOS than those of LNMO. This is also strongly associating with the lowered overpotential for the redox reaction of Ni^{2+}/Ni^{3+}. These are due to the hybridization of S-3p orbital and Ni-3d one, and it is considered that the contribution of covalent bond was enhanced by the S substitution. Schematic diagrams summarizing the above considerations are shown in supplementary Fig.S6(b). Figure S6b was drawn as a diagram to understand the overall picture of changes in electronic structure. Incorporation of S^{2-} into the spinel lattice slightly increased the bottom of the Ni-3d (t2g) bloc, comparing to that of original oxide. In contrast, the shift in the bottom in the Fermi energy was found to be significantly higher of 0.69 eV. Based on these theoretical facts, we thought that the overall shift of Ni-3d was not happen, significantly.

Electrochemical impedance spectroscopy (EIS) and Galvanostatic intermittent titration technique (GITT) were further performed to examine kinetic parameters (Fig. 4b and Fig. S7). The high- and medium-frequency semicircles represent surface film resistance (R_{sf}) and charge transfer resistance (R_{ct}), respectively, at the electrode–electrolyte interface. The kinetical parameters were analyzed using an equivalent electrical circuit model and are summarized in Table S3. Lithium ion diffusion coefficients (D$_{Li}$) of the porous LNMO cathodes were slightly increased by the incorporation of S^{2-} onto the surface. It is interestingly note that the R$_{sf}$ was increased with increasing S^{2-} content, even though the R_{ct} was degraded with increasing S^{2-}

content. These two different trends are symbolic characteristics that show the impacts of oxysulfide surfaces on electrode reactions. Furthermore, GITT spectra also represented that Li$^+$ diffusion coefficient (D$_{Li}$) was slightly increased by the S^{2-} incorporation. The changes in the D$_{Li}$ responding to the SOCs, represented similar trends without any dependence with S^{2-} incorporation. It was enhanced in proportional to the SOC by 4.6 V. These results suggest that the oxysulfide surface does not provide significant impacts on various resistance processes formed in the porous cathode at different SOC. Thus, the oxysulfide surface will be considered to primarily contribute to the CEI layer characteristics for the enhancement of battery performances, including thickness and conductivity, of which they are independent on the SOC of cathodes.

The trajectory of Li$^+$ migration within spinel framework and the corresponding activation energy were probed by DFT calculations in order to understand the S^{2-} substitution effects of Li$^+$ diffusion behavior. Lithium ion preferentially migrated along the tetrahedral 8c– octahedral 4a/12d– tetrahedral 8c route with the energy profiles of Li$^+$ hopping paths with lowest activation energies irrespective of the extent of S^{2-} substitution (Fig. 4c, d). The activation barrier for Li$^+$ hopping in the LNMO and series of LNMOS$_x$ crystals became the smallest in the 4a model at $x = 0.125$ (1.2 eV) and 12d-3 model at $x = 0.25$ (0.7 eV), respectively. In particular, the LNMOS$_{0.15}$ crystal showed lower activation energies for the self-diffusion than those of LNMOS$_{0.1}$ crystal, which was in good agreement with the C-rate capability test (Fig. 4a). However, their activation energies were still very high, as comparing to those of stoichiometric LNMO, nonstoichiometric LNMO$_{4-\delta}$, and LNMOF$_x$.[30] Their trajectories of Li$^+$ hopping along migration paths summarized in Fig. 4c, d suggests that the migration path and activation energy of Li$^+$ hopping basically depend on the interaction between V'_{Li} at the 8c-4a/12d-8c sites and O or $S_0^\times$ at the 24e sites, similarly to the cases of LNMOF$_x$ crystals.[30] The Li$^+$ in stoichiometric LNMO was transported in a straight line along the migration path. In contrast, Li$^+$ in LNMOS$_{0.1}$ migrates tortuously at near $S_0^\times$ due to its larger ionic radius. Based on the above theoretical insights, one can conclude that octahedral vacancy shape and volume, which are strongly affected by the substitution environment, significantly influence the dynamics of Li$^+$ migration. We think that the energy barrier for Li$^+$ hopping is increased by the reduction of octahedral vacancy volume by the introduction of S^{2-} with lager ionic radius into the Li$^+$ diffusion path. Such significant influence of resistive component for Li$^+$ transport inside the active materials might have made the R$_{sf}$ of the LNMOS$_x$ crystal electrodes higher, comparing to that of LNMO and LNMOF$_x$.

A cyclability test will be critical for understanding the impact of SEI layer in accordance with the impedance growth. The LNMO and LNMOS$_x$ electrodes-based half cells were cycled for 200 cycles at 25 ^{o}C with current density of 150 mA·g^{-1} corresponding to 1 C (Fig. 5a). A significant capacity loss with cycle number was observed to 79% of the initial capacity for the LNMO/Li half cells after 200 cycles. The LNMOS$_x$/Li half cells showed an obvious improvement in the cyclability with capacity retentions >90%. Moreover, the highly substituted LNMOS$_{0.15}$ electrodes showed the highest capacity retention of 95% among all prepared electrodes. The coulombic efficiency of the cell was almost

ARTICLE

constant at >99% after the second cycles. Furthermore, EIS experiments for the cells after 200 cycles showed that all the kinetic parameters in LNMO/Li cell degraded with cycling (Fig. 5b), however, the deterioration of the LNMOS$_x$/Li cell was significantly smaller (Table S3). Furthermore, variation of electrochemical resistance was decreased with increasing sulfur content. LNMOS$_{0.15}$ electrode presented a noticeable small degradation in R_{sf} and R_{ct}. Moreover, the lithium ion diffusion coefficient inside the porous LNMOS$_{0.15}$ composite electrode became higher after cycles.

Further investigation on the chemical state of the cycled electrodes surface was performed using X-ray photoelectron spectroscopy (XPS) to determine the influence of oxysulfide surface on SEI formation reaction. Fig. 5c shows the depth profile of C1s core-level spectra for the 200 cycled electrodes. The cycled LNMO electrode displayed obvious different spectral characteristics compared to those of the LNMOS$_x$ electrodes. The broaden spectrum peak observed with LNMO electrode was individually detected into multiple components with LNMOS$_x$ electrodes. In particular, the peak area belonging to C=O/O–C–O bonds had dramatically decreased with LNMOS$_x$ electrodes. Furthermore, the C=O/O–C–O bonds were detected from the LNMO electrode even after removing the surface SEI layer corresponding to a thickness of 20 nm in terms of silicon by Ar sputtering, while LNMOS$_x$ electrodes presented absence of C=O/O–C–O bonds (Fig. 5d). Similar trends were recognized in O1s core level spectra (Fig. 5e, f). In addition, the incorporation of S^{2-} on the LNMO surface was found to substantially decrease the peak area centered at 535.8 eV which is attributed to Li$_x$PF$_y$O$_z$. Since Li$_x$PF$_y$O$_z$ is known to generate from Lewis acidic PF^{5-} which was from the decomposition of LiPF$_6$ salt at the electrode surface, the LNMO electrode surface is considered to have Lewis base nature toward LiPF$_6$ salt. If an oxide has certain properties because it is a Lewis base, these properties can be suppressed by adsorbing a Lewis acid on the surface[49]. These facts strongly suggest that the incorporation of S^{2-} into the LNMO surface atomic layer might mitigate its Lewis base characteristics, leading to inhibiting the decomposition of the LiPF$_6$ at the surface. The XPS-Mn 2p core level spectra of the as cycled and after sputtered electrodes are shown in Fig. S7a, b. No significant changes in the peak intensity ratio of Mn^{3+}/Mn^{4+} was observed in the cycled LNMOS$_x$ electrodes in contrast to that of bare LNMO. Since the absence ratio of Mn^{3+} was sufficiently retained in the LNMO stabilized with the incorporation of S^{2-}, Mn^{3+} does not go through the notorious disproportionation reaction. These spectral features also support our consideration of the impact of the incorporation of S^{2-} on mitigating unexpected excess SEI layer growth.

Furthermore, XPS valence band spectroscopy and Ultraviolet photoelectron (UPS) measurements were performed to determine the electronic structure of the LNMOS$_x$ electrode surface. The valence band edge positions apparently shifted to deeper levels, while the corresponding peak areas decreased due to the oxysulfide surface formation (Fig. 5g). Since a similar shift of the valence band edge position was observed for both the LNMOF$_x$ electrode surface[32], and fluoroalkylsilane monolayer immobilized LNMO$_{4-\delta}$ electrode surface, those which delivered significant improvement of high-voltage durability.[28,29] This

implies that the incorporation of S^{2-} stabilized the Ni–Ni, Mn–Mn and O–O bonds located on the top surface of LNMO crystals, thus preventing gas evolution, transition metals ion dissolution, and the formation of an excessive SEI layer. DFT calculation evaluated the PDOS peaks located near the Fermi level were shifted to lower energies after the incorporation of S^{2-}, which was consistent with the results of XPS valence band measurements. Ultraviolet photoelectron measurements were also performed to elucidate the effect of the oxysulfide surface formation on its ionization potential. As shown in Fig. 5h, the threshold of the ultraviolet light energy required for the generation of a photoelectron from the LNMO electrode surface increased, and the number of produced photoelectrons decreased in the LNMOS$_x$ electrodes as the increase of S^{2-} contents. The observed spectral characteristics also strongly suggest that the formation of oxysulfide surface on LNMO crystals increased the energy difference between the Fermi level and the vacuum level. Moreover, the presence of S^{2-} in the LNMO surface significantly decreased the probability of the reduction of both Ni and Mn ions via the oxidative decomposition of the electrolyte at a high voltage. All these experimental results evidentially indicate that sulfur anion incorporated on the LNMO surface atomic layer provides positive impacts for suppressing the formation of metal fluoride as a solid electrolyte interface and the dissolution of transition metals ion in the electrolyte due to the oxidative decomposition of the liquid electrolyte at high voltage. It is thought that the thinner SEI layer formation on the oxysulfide surface might promote efficient diffusion of Li$^+$ at an electrolyte interface, which results in the decrease trend of the R_{ct} in the LNMOS$_x$ electrodes-based half-cells. As a result, we concluded that the oxysulfide surface with lower Lewis base characteristics strongly contributes to preventing the risk for higher capacity fading at high-voltage operation because of the occurrence of a short circuit caused by transition metals dissolution during cycling.

Conclusions

This systematic study using experimental and theoretical approaches has ascribed many new insights regarding the oxysulfide surface effects on structural and electrochemical characteristics in high-voltage spinel LNMO electrodes. Carbothermal reaction using sulfur-doped hydrocarbons (S-HC) particles as precursors made it possible to incorporate S^{2-} ions into the LNMO surface. It will contribute to academic knowledge regarding the multi-anion surface effects on the side reaction that appeared at the electrolyte interface, as well as the diffusion behaviour of Li$^+$ ions inside the electrodes. Compared with the oxyfluoride surfaces reported previously,[32] the oxysulfide surface provided high cyclability and no impedance growth due to the thinner SEI layer formation. However, the oxysulfide surface provided poor output characteristics due to the ionic radius of S^{2-} being larger than O^{2-} and F$^-$. In a lithium ion compound crystal system having a small lattice volume, it is difficult to maintain a sufficient space necessary for lithium ion diffusion. Therefore, in contrast to a lithium-ion battery material, sodium-ion battery materials with a larger lattice

volume will potentially show better compatibility for the incorporation of S^{2-} ions into the lattice. We believe that multi-anion surfaces will provide many new possibilities for materials design concepts for improving battery performances by managing side reactions that occur at the electrolyte–electrode interface.

Conflicts of interest

There are no conflicts to declare.

Acknowledgements

Notes and references

1 M. Li, J. Lu, Z. Chen, K. Amine, 30 Years of Lithium-Ion Batteries. *Adv. Mater.* 2018, **30**, 1800561.

2 P. K., Nayak, E. M. Erickson, F. Schipper, T. R. Penki, N. Munichandraiah, P. Adelhelm, H. Sclar, F. Amalraj, B. Markovsky, D. Aurbach, Review on Challenges and Recent Advances in the Electrochemical Performance of High Capacity Li- and Mn-Rich Cathode Materials for Li-Ion Batteries. *Adv. Energy Mater.* 2018, **8**, 1702397.

3 X. Feng, M. Ouyang, X. Liu, L. Lu, Y. Xia, X. He, Thermal Runaway Mechanism of Lithium Ion Battery for Electric Vehicles: a Review. *Energy Storage Mater.* 2018, **10**, 246–267.

4 G. Zubi, R. Dufo-López, M. Carvalho, G. Pasaoglu, The Lithium-Ion Battery_ State of the Art and Future Perspectives. *Renew. Sustain. Energy Rev.* 2018, **89**, 292–308.

5 T. F. Yi, J. Mei, Y. R. Zhu, Key Strategies for Enhancing the Cycling Stability and Rate Capacity of $LiNi_{0.5}Mn_{1.5}O_4$ as High-Voltage Cathode Materials for High Power Lithium-Ion Batteries. *J. Power Sources* 2016, **316**, 85–105.

6 X. Xu, S. Deng, H. Wang, J. Liu, H. Yan, Research Progress in Improving the Cycling Stability of High-Voltage $LiNi_{0.5}Mn_{1.5}O_4$ Cathode in Lithium-Ion Battery. *Nano-Micro Letters* 2016, **9**, 1–19.

7 Y. Qiao, Y. He, K. Jiang, Y. Liu, X. Li, M. Jia, S. Guo, H. Zhou, High-Voltage Li-Ion Full-Cells with Ultralong Term Cycle Life at Elevated Temperature. *Adv. Energy Mater.* 2018, **8**, 1802322.

8 A. Manthiram, K. Chemelewski, E. S. Lee, A Perspective on the High-Voltage $LiMn_{1.5}Ni_{0.5}O_4$ Spinel Cathode for Lithium-Ion Batteries. *Energy Environ. Sci.* 2014, **7**, 1339–1350.

9 K. R. Chemelewski, D. W. Shin, W. Li, W.; Manthiram, A. Octahedral and Truncated High-Voltage Spinel Cathodes: the Role of Morphology and Surface Planes in Electrochemical Properties. *J. Mater. Chem. A* 2013, **1**, 3347–3354.

10 N. N. Intan, K. Klyukin, V. Alexandrov, Theoretical Insights Into Oxidation States of Transition Metals at (001) and

(111) $LiNi_{0.5}Mn_{1.5}O_4$ Spinel Surfaces. *J. Electrochem. Soc.* 2018, **165**, A1099–A1103.

11 J. Ma, P. Hu, G. Cui, L. Chen, Surface and Interface Issues in Spinel $LiNi_{0.5}Mn_{1.5}O_4$: Insights Into a Potential Cathode Material for High Energy Density Lithium Ion Batteries. *Chem. Mater.* 2016, **28**, 3578–3606.

12 N. Kumar, K. Leung, D. J. Siegel, Crystal Surface and State of Charge Dependencies of Electrolyte Decomposition on $LiMn_2O_4$ Cathode. *J. Electrochem. Soc.* 2014, **161**, E3059–E3065.

13 K. Leung, First-Principles Modeling of Mn(II) Migration Above and Dissolution From $LixMn_2O_4$ (001) Surfaces. *Chem. Mater.* 2016, **29**, 2550–2562.

14 J. W. Kim, D. H. Kim, D. Y. Oh, H. Lee, J. H. Kim, J. H., Lee, Y. S. Jung, Surface Chemistry of $LiNi_{0.5}Mn_{1.5}O_4$ Particles Coated by Al_2O_3 Using Atomic Layer Deposition for Lithium-Ion Batteries. *J. Power Sources* 2015, **274**, 1254–1262.

15 S. Tao, F. Kong, C. Wu, X. Su, T. Xiang, S. Chen, H. Hou, L. Zhang, Y. Fang, Z. Wang, Nanoscale TiO_2 Membrane Coating Spinel $LiNi_{0.5}Mn_{1.5}O_4$ Cathode Material for Advanced Lithium-Ion Batteries. *J. Alloys Compd.* 2017, **705**, 413–419.

16 J. S. Chae, S.-B. Yoon, W.-S., Yoon, Y.-M. Kang, S.-M. Park, J.-W. Lee, K. C. Roh, Enhanced High-Temperature Cycling of $Li_2O-B_2O_3$-Coated Spinel-Structured $LiNi_{0.5}Mn_{1.5}O_4$ Cathode Material for Application to Lithium-Ion Batteries. *J. Alloys Compd.* 2014, **601**, 217–222.

17 M. Gellert, K. I. Gries, J. Sann, E. Pfeifer, K. Volz, Roling, B. Impedance Spectroscopic Study of the Charge Transfer Resistance at the Interface Between a $LiNi_{0.5}Mn_{1.5}O_4$ High-Voltage Cathode Film and a $LiNbO_3$ Coating Film. *Solid State Ionics* 2016, **287**, 8–12.

18 S. Chae, J. Soon, H. Jeong, T.-J. Lee, J. H. Ryu, S. M. Oh, Passivating Film Artificially Built on $LiNi0.5Mn1.5O4$ by Molecular Layer Deposition of (Pentafluorophenylpropyl)Trimethoxysilane. *J. Power Sources* 2018, **392**, 159–167.

19 M. Xu, L. Zhou, Y. Dong, Y. Chen, A. Garsuch, B. L. Lucht, Improving the Performance of Graphite/LiNi0. 5Mn1. 5O4 Cells at High Voltage and Elevated Temperature with Added Lithium Bis (Oxalato) Borate (LiBOB). *J. Electrochem. Soc.* 2013, **11**, A2005–A2013.

20 Z. Liu, P. Hu, J. Ma, B. Qin, Z. Zhang, C. Mou, Y. Yao, G. Cui, Conformal Poly(Ethyl a-Cyanoacrylate) Nano-Coating for Improving the Interface Stability of $LiNi_{0.5}Mn_{1.5}O_4$. *Electrochim. Acta* 2017, **236**, 221–227.

21 W. K. Pang, H. F. Lin, V. K. Peterson, C.-Z. Lu, C.-E. Liu, S.-C. Liao, J.-M. Chen, Enhanced Rate-Capability and Cycling-Stability of 5 V SiO_2- And Polyimide-Coated Cation Ordered $LiNi_{0.5}Mn_{1.5}O_4$ Lithium-Ion Battery Positive Electrodes. *J. Phys. Chem. C* 2017, **121**, 3680–3689.

22 S. Solchenbach, M. Wetjen, D. Pritzl, K. U. Schwenke, H. A. Gasteiger, Lithium Oxalate as Capacity and Cycle-Life Enhancer in LNMO/Graphite and LNMO/SiG Full Cells. *J. Electrochem. Soc.* 2018, **165**, A512–A524.

23 M. Gauthier, T. J. Carney, A. Grimaud, L. Giordano, N. Pour, H.-H. Chang, D. P. Fenning, S. F. Lux, O. Paschos, C. Bauer, C.; *et al.* Electrode–Electrolyte Interface in Li-Ion Batteries: Current Understanding and New Insights. *J. Phys. Chem. Lett.* 2015, **6**, 4653–4672.

24 P. Peljo, H. H. Girault, Electrochemical Potential Window of Battery Electrolytes: the HOMO-LUMO Misconception. *Energy Environ. Sci.* 2018, **11**, 2306–2309.

25 L. Cheng, R. S. Assary, X. Qu, A. Jain, S. P. Ong, N. N. Rajput, K. Persson, L. A. Curtiss, Accelerating Electrolyte Discovery for Energy Storage with High-Throughput Screening. *J. Phys. Chem. Lett.* 2015, **6**, 283–291.

26 K. Xu, Electrolytes and Interphasial Chemistry in Li Ion Devices. *Energies* 2010, **3**, 135–154.

27 N. Zettsu, S. Kida, S. Uchida, K. Teshima, Sub-2nm Thick Fluoroalkylsilane Self-Assembled Monolayer-Coated High Voltage Spinel Crystals as Promising Cathode Materials for Lithium Ion Batteries. *Sci. Rep.* 2016, **6**, 31999.

28 D.-W. Kim, S. Uchida, H. Shiiba, N. Zettsu, K. Teshima, New Insight for Surface Chemistries in Ultra-Thin Self-Assembled Monolayers Modified High-Voltage Spinel Cathodes. *Sci. Rep.* 2018, **8**, 11771.

29 D.-W. Kim, H. Shiiba, N. Zettsu, T. Yamada, T. Kimijima, G. S. Santolino, R. Ishikawa, Y. Ikuhara, K. Teshima, Full Picture Discovery for Mixed-Fluorine Anion Effects on High-Voltage Spinel Lithium Nickel Manganese Oxide Cathodes. *NPG Asia Mater.* 2017, 9, e398.

30 S. Cho, J.W. Jang, K. J. Kong, E. S. Kim, K. H. Lee, J. S. Lee, Anion-Doped Mixed Metal Oxide Nanostructures Derived From Layered Double Hydroxide as Visible Light Photocatalysts. *Adv. Funct. Mater.* **2013**, *23*, 2348–2356.

31 N. C. Birben, C. S. Uyguner-Demirel, S. Sen-Kavurmaci, Y. Y. Gürkan, N. Türkten, M. Kılıç, Z. Çınar, M. Bekbolet, Photocatalytic Performance of Anion Doped TiO_2 On the Degradation of Complex Organic Matrix. *J. Adv. Oxid. Technol.* 2016, **19**, 199–207.

32 F. Kong, C. Liang, R. C. Longo, D.-H. Yeon, Y. Zheng, J.-H. Park, J.-H.; Doo, S.-G.; Cho, K. Conflicting Roles of Anion Doping on the Electrochemical Performance of Li-Ion Battery Cathode Materials. *Chem. Mater.* 2016, **28**, 6942–6952.

33 A. Wei, W. Li, Q. Chang, X. Bai, R. He, L. Zhang, Z. Liu, Y. Wang, Effect of Mg^{2+}/F^- Co-Doping on Electrochemical Performance of $LiNi_{0.5}Mn_{1.5}O_4$ For 5V Lithium-Ion Batteries. *Electrochim. Acta* 2019, **323**, 134692.

34 Y. Charles-Blin, D. Flahaut, J.-B. Ledeuil, K. Guérin, M. Dubois, N. Louvain, L. Monconduit, H. Martinez, Surface Layer Fluorination of TiO_2 Electrodes for Electrode Protection LiBs: Fading the Reactivity of the Negative Electrode/Electrolyte Interface. *J. Electrochem. Soc.* 2019, **166**, 1905–1914.

35 D.-W. Kim, O. L. Li, N. Saito, Enhancement of ORR Catalytic Activity by Multiple Heteroatom-Doped Carbon Materials. *Phys. Chem. Chem. Phys.* 2015, **17**, 407–413.

36 G. Kresse, J. Furthmüller, Efficiency of ab-initio total energy calculations for metals and semiconductors using a plane-wave basis set. *Comput. Mater. Sci.* 1996, **6**, 15–50.

37 G. Kresse, J. Furthmüller, Efficient interative schemes for ab initio total-energy calculations using a plane-wave basis set. *Phys. Rev. B* 1996, **54**, 11169–11186.

38 J. P. Perdew, A. Ruzsinszky, G. I. Csonka, O. A. Vydrov, G. E. Scuseria, L. A. Constantin, X. Zhou, K. Bruke, Restoring the Density-Gradient Expansion for Exchange in Solids and Surfaces. *Phys. Rev. Lett.* 2008, **100**, 136406.

39 P. E. Blöchl, Projector augmented-wave method. *Phys. Rev. B* 1994, **50**, 17953–27.

40 A. Jain, G. Hautier, S. P. Ong, C. J. Moore, C. C. Fischer, K. A. Persson, G. Ceder, Formation enthalpies by mixing GGA and GGA +U calculations. *Phys. Rev. B* **2011**, 84, 66–11.

41 T. Mueller, G. Hautier, A. Jain, G. Ceder, Evaluation of Tavorite-Structured Cathode Materials for Lithium-Ion Batteries Using High-Throughput Computing. *Chem. Mater.* 2011, **23**, 3854–3862.

42 G. Hautier, S. P. Ong, A. Jain, C. J. Moore, G. Ceder, Accuracy of density functional theory in predicting formation energies of ternary oxides from binary oxides and its implication on phase stability. *Phys. Rev. B* 2012, **85**, 973–19.

43 N. Biškup, J. L. Martínez, D. Arroyo, P. Díaz-Carrasco,J. Morales, Relation between the magnetic properties and the crystal and electronic structures of manganese spinels $LiNi_{0.5}Mn_{1.5}O_4$ and $LiCu_{0.5}Mn_{1.5}O_{4-\delta}$ $(0<\delta<0.125)$. *J. Appl. Phys.* 2006, **100**, 093908.

44 N. Amdouni, K. Zaghib, F. Gendron, A. Mauger, C. M. Julien, Magnetic properties of $LiNi_{0.5}Mn_{1.5}O_4$ spinels prepared by wet chemical methods. *J. Magn. Magn. Mater.* 2007, **309**, 100–105.

45 Y. Chen, Y. Sun, X. Huang, Origin of the Ni/Mn ordering in high-voltage spinel $LiNi_{0.5}Mn_{1.5}O_4$: The role of oxygen vacancies and cation doping. *Comput. Mater. Sci.* 2016, **115**, 109–116.

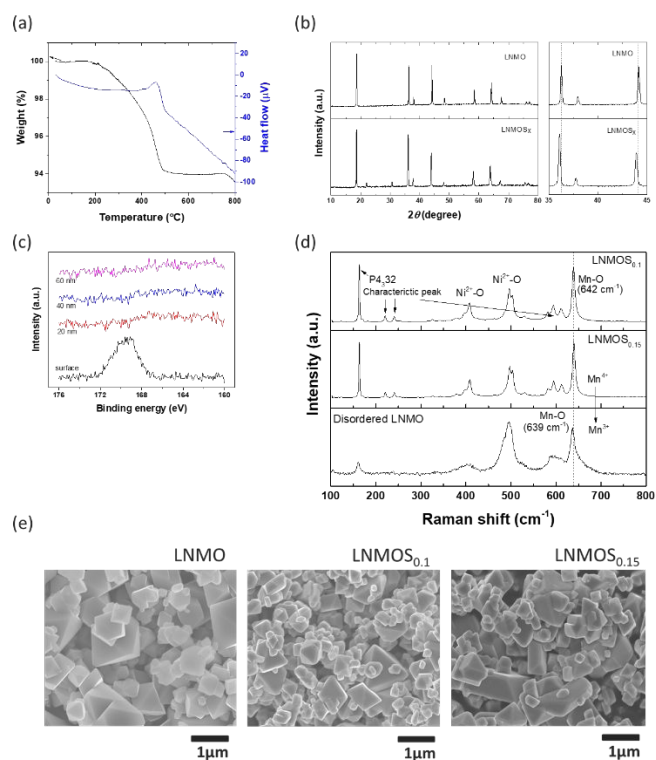46 P. W. Tasker, The stability of ionic crystal surface. *J. Phys. C.* **1979**, 12, 4977–4984.

Figure 1. Structural characteristics of LNMO, series of LNMOS$_x$ crystals were summarized: (a) TG-DTA profiles of the mixture of S-HC powders (0.045 g) and LNMO crystal (0.955 g) which are responsible for LNMOS$_{0.1}$ crystal formation, (b) The powder XRD patterns, (c) Depth profiles of XPS-S3p core-level spectra as a function of Ar sputtering, (d) Raman spectra, and (e) FE-SEM images.
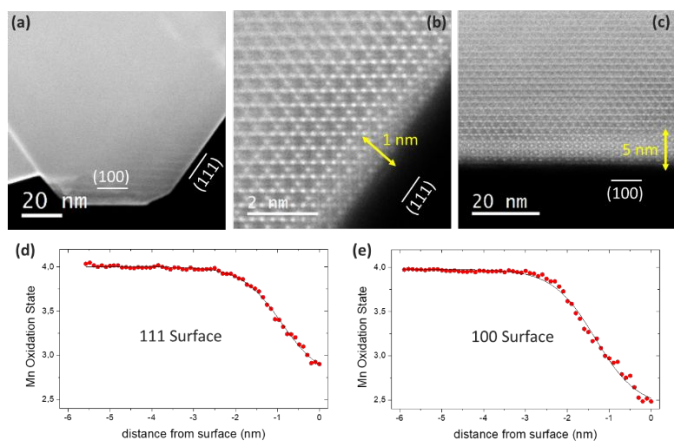
Figure 2. Characterization of surface atomic structure of LNMOS$_{0.15}$. (a) STEM images and annular bright-field STEM (ABF-STEM) images of (b) (111) and (c) (100) surface. (d and e) Mn oxidation state as a function of distance from the surface by EELS Mn-L2,3 edges.
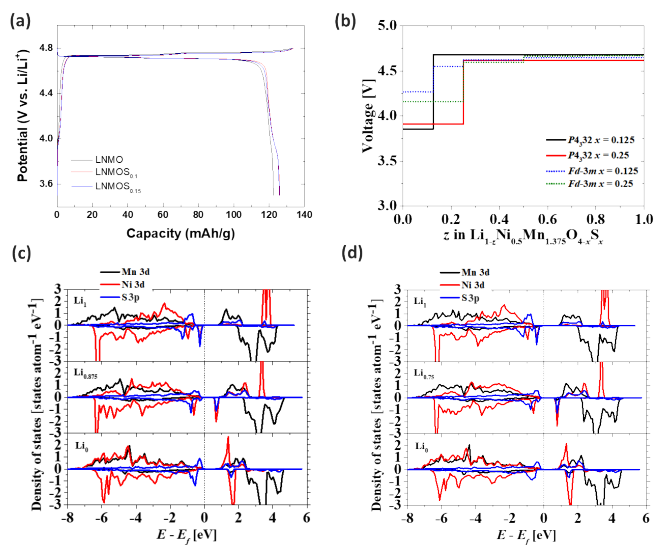
Figure 3. Electrochemical impact of S^{2-} substitution. (a) galvanostatic charge–discharge curves in the range of 3.5–4.8 V at 0.2 C-rate, (b) computationally predicted voltage profiles of LNMO and LNMOS$_x$ during the charging reaction as a function of Li content. DFT calculations on the changes in partial density of states (PDOS) for Ni-3d, Mn-3d and S-3p orbitals: (c) x = 0.125, and (d) x = 0.25.
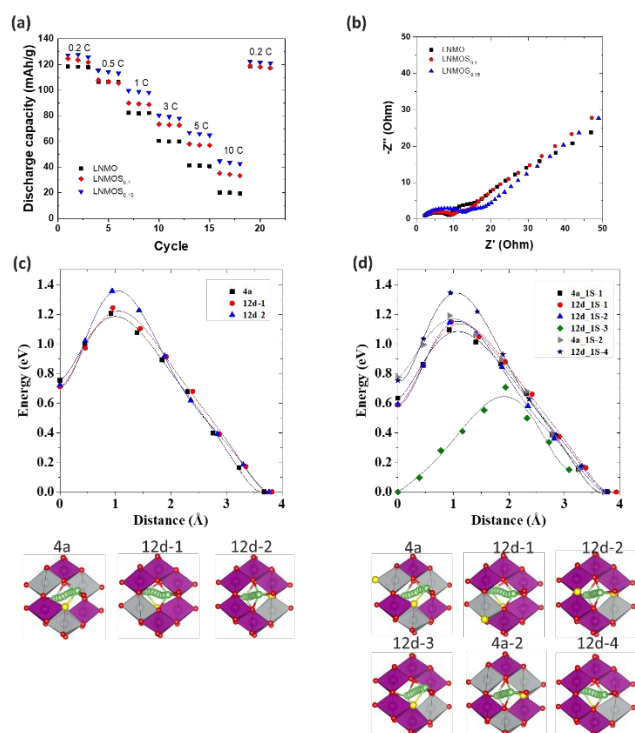
Figure 4. Lithium ion transportational characteristics in the LNMO/Li, and LNMOS$_x$/Li half cells. (a) C-rate capabilities and (b) Nyquist plots. (c, d) Computationally predicted possible Li+ migration paths and their energy profiles for (c) LNMOS$_{0.125}$ and (d) LNMOS$_{0.25}$
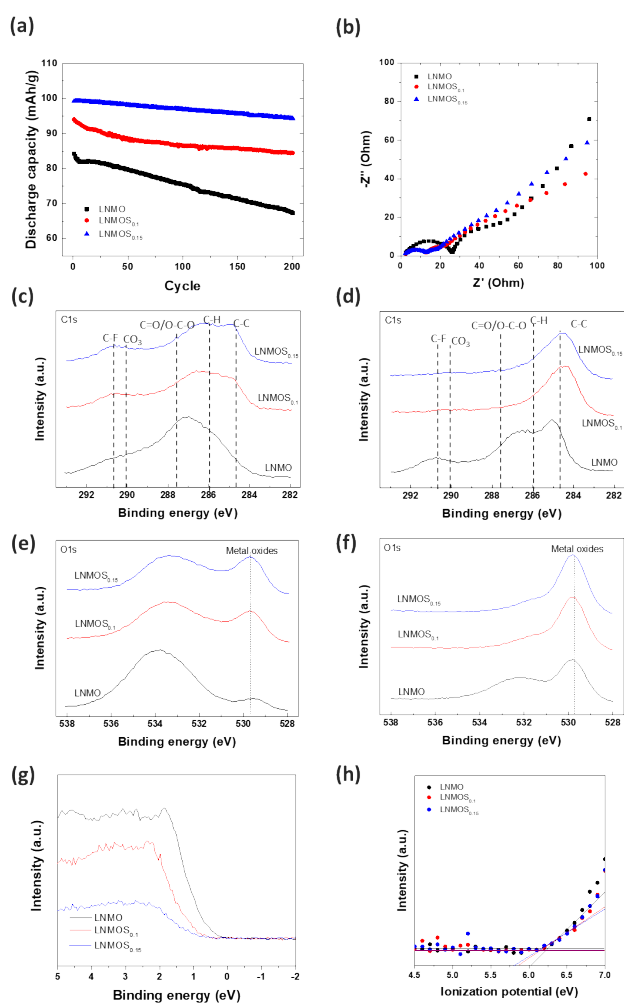
Figure 5. (a) Plots of discharge capacity vs. cycle number for LNMO/Li and LNMOS$_x$/Li cells operated at 1 C in a cut-off voltage window of 2.5–4.8 V, and (b) EIS characterizations were followed after 200 cycles. (c, d) C1s, and (e,f) O1s XPS core-level spectra of 200 cycled LNMO and LNMOS$_x$ electrodes taken from as prepared surface (c, e), and following Ar sputtered surface (d, f). (g) XPS valence band spectra and (h) ionization potential of the fresh LNMO and LNMOS$_x$ electrodes.